

Numerical Simulation of the Red Sea Outflow Using HYCOM and Comparison with REDSOX Observations

YEON S. CHANG, TAMAY M. ÖZGÖKMEN, HARTMUT PETERS, AND XIAOBIAO XU

RSMAS/MPO, University of Miami, Miami, Florida

(Manuscript received 11 September 2006, in final form 2 March 2007)

ABSTRACT

The outflow of warm, salty, and dense water from the Red Sea into the western Gulf of Aden is numerically simulated using the Hybrid Coordinate Ocean Model (HYCOM). The pathways of the modeled overflow, temperature, salinity, velocity profiles from stations and across sections, and transport estimates are compared to those observed during the 2001 Red Sea Outflow Experiment. As in nature, the simulated outflow is funneled into two narrow channels along the seafloor. The results from the three-dimensional simulations show a favorable agreement with the observed temperature and salinity profiles along the channels. The volume transport of the modeled overflow increases with the increasing distance from the southern exit of the Bab el Mandeb Strait due to entrainment of ambient fluid, such that the modeled transport shows a reasonable agreement with that estimated from the observations. The initial propagation speed of the outflow is found to be smaller than the estimated interfacial wave speed. The slow propagation is shown to result from the roughness of the bottom topography characterized by a number of depressions that take time to be filled with outflow water. Sensitivities of the results to the horizontal grid spacing, different entrainment parameterizations, and forcing at the source location are investigated. Because of the narrow widths of the approximately 5 km of the outflow channels, a horizontal grid spacing of 1 km or less is required for model simulations to achieve a reasonable agreement with the observations. Comparison of two entrainment parameterizations, namely, TPX and *K*-profile parameterization (KPP), show that similar results are obtained at 1-km resolution. Overall, the simulation of the Red Sea outflow appears to be more strongly affected by the details of bottom topography and grid spacing needed to adequately resolve them than by parameterizations of diapycnal mixing.

1. Introduction

Most deep and intermediate water masses of the World Ocean originate via overflows from marginal and polar seas. While flowing down the continental slope, these water masses entrain ambient waters such that the turbulent mixing strongly modifies the temperature (T), salinity (S), and equilibrium depth of the so-called product water masses. As the mixing takes place over small space and time scales, it needs to be parameterized in ocean general circulation models (OGCMs). OGCMs are found to be highly sensitive to details of the representation of overflows in these models (e.g., Willebrand et al. 2001), and the entrainment of ambient waters into overflows has been recognized to

have significant impact on the ocean general circulation, and possibly on climate. Based on this recognition, our ongoing work within the concept of the “Climate Process Team on Gravity Current Entrainment” (<http://www.cpt-gce.org/>) aims to address the following questions:

- (i) What are the factors influencing entrainment in overflows?
- (ii) How do these factors differ in a variety of overflows in the World Ocean?
- (iii) How can these factors be incorporated into parameterizations for OGCMs?

Because of the importance of overflows, there has been significant observational work [e.g., Baringer and Price (1997a,b) for the Mediterranean Sea outflow; Girton and Sanford (2003) and Girton et al. (2001) for the Denmark Strait overflow; Peters et al. (2005) and Peters and Johns (2005) for the Red Sea outflow; and Gordon et al. (2004) for outflows from the Antarctic

Corresponding author address: Tamay M. Özgökmen, RSMAS/MPO, University of Miami, 4600 Rickenbacker Causeway, Miami, FL 33149.

E-mail: tozgokmen@rsmas.miami.edu

shelves]. The entrainment into gravity currents has also been studied in laboratory tank experiments (e.g., Ellison and Turner 1959; Britter and Linden 1980; Simpson 1969, 1982, 1987; Turner 1986; Hallworth et al. 1996; Monaghan et al. 1999; Baines 2001, 2005; Cenedese et al. 2004) as well as in numerical process studies (Özgökmen and Chassignet 2002; Özgökmen et al. 2003, 2004a,b, 2006; Ezer and Mellor 2004; Ezer 2005, 2006; Legg et al. 2006).

One of the most challenging issues about modeling overflows is development of physically based and realistic entrainment parameterizations. It is generally accepted that entrainment in overflows results from shear instability. Thus it is logical to explore how the entrainment to the local gradient Richardson number $Ri = N^2/S^2$, the ratio of the square of buoyancy frequency and vertical shear. Such simple, algebraic, one-equation parameterizations are particularly suitable for climate models to avoid computationally expensive integration of additional prognostic equations (e.g., for turbulent kinetic energy). Fernando (1991) and Strang and Fernando (2001) review such attempts. The frequently used *K*-profile parameterization (KPP; Large et al. 1994; Large and Gent 1999) falls into this category. An entrainment parameterization especially suitable for isopycnic-coordinate ocean models, so-called TP was developed by Hallberg (2000) who adapted a formulation based on bulk Richardson numbers by Ellison and Turner (1959) and Turner (1986). This approach was further developed and fine-tuned by Chang et al. (2005) and Xu et al. (2006), papers on which we build herein.

Possibly because of the problem of realistic mixing parameterizations and of significant demands concerning the spatial model resolution, there has only been a limited number of regional ocean simulations of overflows to date. The outflow from the Mediterranean was modeled by Jungclaus and Mellor (2000), Papadakis et al. (2003), and Xu et al. (2006); the Denmark Strait overflow was simulated by Käse et al. (2003); while Ezer (2006) and Riemenschneider and Legg (2007) recently conducted numerical studies of the Faroe Bank Channel overflow. Thus, the requirements necessary to capture the dynamics of different overflow systems using large-scale models have not been explored in detail.

Herein, the main objective of this study is to carry out a regional simulation of a less modeled overflow, the Red Sea overflow, using an OGCM and to compare the results to the observations collected during the Red Sea Outflow Experiment (REDSOX; Bower et al. 2002, 2005; Peters et al. 2005; Peters and Johns 2005; Matt and Johns 2007). The REDSOX data allow us to initialize, force, and validate our numerical model simulations. While Özgökmen et al. (2003) used a two-di-

mensional, nonhydrostatic model to simulate part of the Red Sea outflow in one of the two outflow channels, the present investigation appears to be the first comprehensive and realistic numerical study of the entire Red Sea outflow system. The secondary objective is that, by carrying out simulations to achieve a reasonable realism, one can then determine the factors necessary for a successful reproduction and modeling of the Red Sea overflow system.

The paper is organized as follows: The principal findings from REDSOX are introduced in section 2. The model configuration, initialization, forcing, and parameters are described in section 3. The results of the simulations are presented in section 4, which is followed by a summary and discussion.

2. The outflow from the Red Sea

The area around the Red Sea is commonly known to be hot and dry, leading to the high salinity of the Red Sea. The densest water in the Red Sea is formed at its northern end in winter when air temperatures are comparatively low (e.g., Morcos 1970; Sofianos et al. 2002). Leaving the Red Sea, dense, warm and salty Red Sea waters flow southward through the topographically complex, 150-km-long, and comparatively narrow strait of Bab el Mandeb, which has a sill depth of 150 m. Although strong tides and wind forcing cause mixing in the strait (Murray and Johns 1997), the salinity of the Red Sea Outflow Water (RSOW) at the southern exit of Bab el Mandeb is usually still close to 40 practical salinity units (psu), a result of early oceanographic surveys (Siedler 1969). The pronounced seasonal variability of the outflow from the Red Sea is a more recent finding; it is a consequence of the monsoon circulation over the northwestern Indian Ocean and adjacent land areas. Another recent finding is the concentration of the outflow south of Bab el Mandeb into two channels (Murray and Johns 1997), the typically 5-km-wide and 130-km-long “northern” channel and the shorter “southern” channel. These channels end at about 800-m depth, beyond which the seafloor slopes steeply into the 1600-m-deep Tadjura Rift, as shown in Fig. 1.

The 2001 Red Sea Outflow Experiment represents the first comprehensive investigation of the near field of RSOW descending to depth south of Bab el Mandeb as well as of its equilibration and further spreading throughout the Gulf of Aden. Results have been described by Bower et al. (2002, 2005), Peters et al. (2005), Peters and Johns (2005), and Matt and Johns (2007)—the latter three papers focusing on the near field most relevant to this study. The instantaneous, local stratification and flow field were measured with a conductivity–temperature–depth probe combined with a lowered

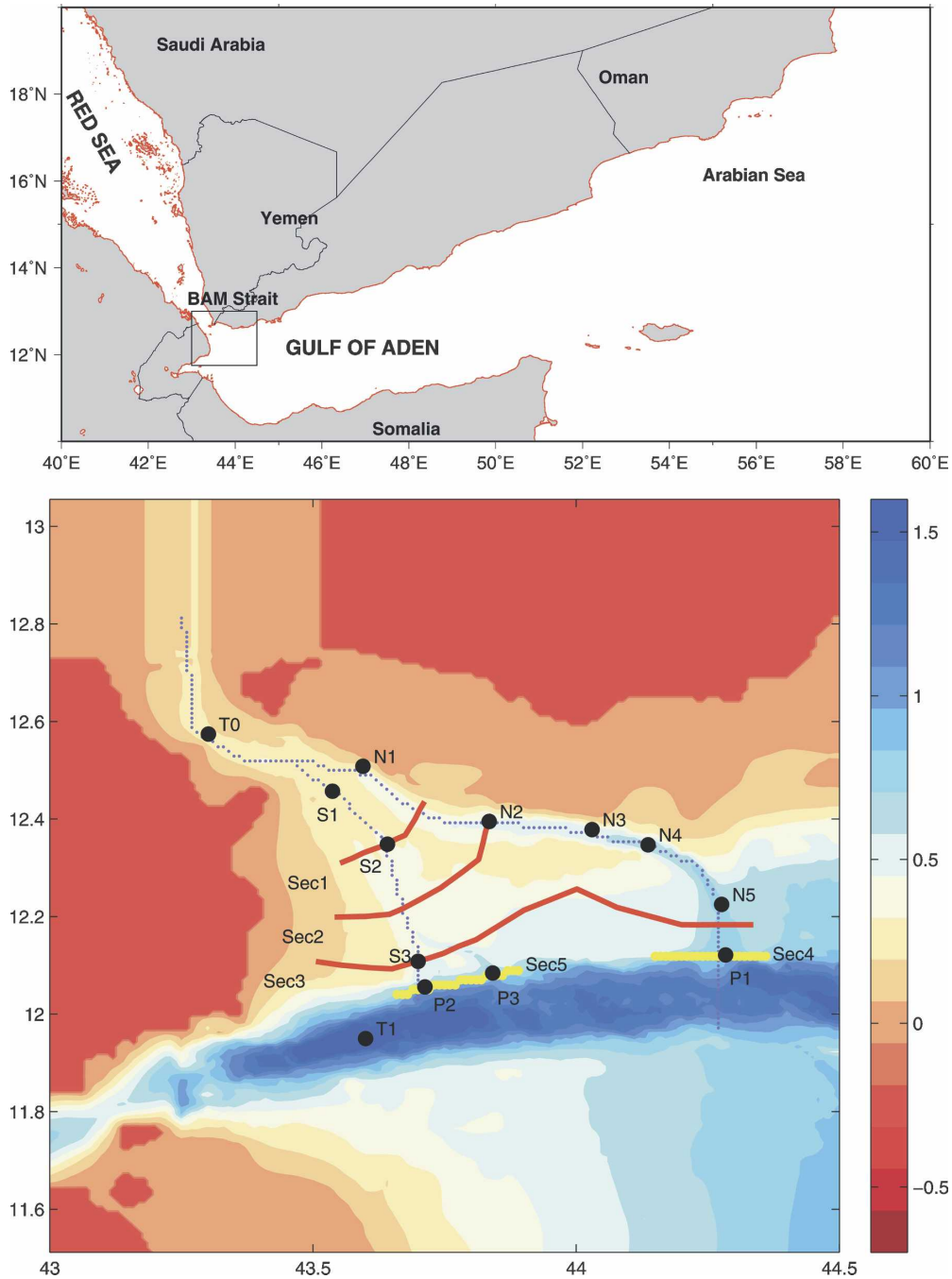


FIG. 1. (top) Chart showing the geographical location of the Red Sea, Bab el Mandeb Strait, and the Gulf of Aden. The box at Bab el Mandeb Strait marks the boundary of the computational domain. (bottom) Enlarged view of the computational domain (in lat and lon). Depths (km) show the bottom topography. The dotted lines indicate the northern and southern channels, the main routes of the Red Sea outflow: T0 denotes the station south of Bab el Mandeb Strait and south of an artificial reservoir created north of 12.7°N. Profiles from T0 are used to validate the source water outflow properties. T1 denotes the station used to initialize the ambient stratification, and it is outside of the outflow pathways. N1–N5 denote the selected measurement locations along the northern channel, and S1–S3 are the selected locations along the southern channel for model validation. In addition, three sections across the outflow plume, sections 1–3, are also used to compare HYCOM results to those from REDSOX.

acoustic Doppler current profiler. Velocity data are referenced to the bottom and are accurate to $\pm 0.03 \text{ m s}^{-1}$ (Peters et al. 2005). While tidal velocities are of the same order as the gravity current in Bab el Mandeb, tidal signals become small, $O(0.05 \text{ m s}^{-1})$, farther downstream (Matt and Johns 2007).

3. The numerical model and computational configuration

In our simulation of the Red Sea outflow we use the Hybrid Coordinate Ocean Model (HYCOM), which allows smoothly varying combinations of depth, density, and terrain-following coordinates. Most relevant for this study is the Lagrangian nature of isopycnic coordinates to naturally migrate with the interface between the descending gravity currents and the ambient fluid, thereby allocating more resolution to locations where most of the entrainment tends to take place. The basic principles of this model are described in Bleck (2002), Chassignet et al. (2003), and Halliwell (2004) and detailed documentation is available online (see <http://hycom.rsmas.miami.edu>).

Based on the information provided in the introduction, the seafloor topography deserves a careful consideration for model configuration. The existence and narrow width of the two channels in the seafloor constrains the pathways and spreading of the overflow. In particular, the bifurcation point where the two channels separate (at approximately 12.5°N , 43.5°E ; Fig. 1) requires a very high-resolution dataset because it can determine the ratio of outflow transports in the two channels. Our model topography is based on multibeam echo soundings taken during REDSOX and a cruise of the French R/V *L'Atalante* (see Hébert et al. 2001). These measurements have a horizontal resolution just below 200 m and cover all areas critical to this study. Remote areas and gaps were filled with the Smith and Sandwell (1997) 2' gridded seafloor data. The 5-minute gridded elevations/bathymetry for the world (ETOPO5) dataset was not found to be accurate when compared to the multibeam measurements and contained critical errors, in particular regarding the bifurcation point of the channels.

The preceding also implies that the model grid spacing is critical. The resolution needs to be fine enough to resolve the two outflow channels with their ~ 5 km width. To examine the role of the horizontal resolution, we vary the grid size from $\Delta x = \Delta y = 5$ km to $\Delta x = \Delta y = 0.5$ km. Note that such resolutions are typical for coastal modeling applications and are considered to be high resolution for regional studies, but they are not feasible in global simulations at the present time. The computational domain covers the region between 11.5°

and 13.1°N , 43° and 44.5°E (Fig. 1). The corresponding number of horizontal grid points ranges from 31×33 to 301×317 . The grid size is only varied in the horizontal directions, while all model experiments have 16 isopycnal layers in the vertical.

Dense overflow water is forced to flow down along the channels as follows. An artificial reservoir is created in the northwest corner of the domain by extending the topography along 12.7°N northward (see Fig. 1). The reservoir is closed along its northern side and does not incorporate any Red Sea or Bab el Mandeb dynamics explicitly. Within the reservoir, the model T - S profiles are relaxed toward profiles taken from the REDSOX observations at Bab el Mandeb Strait using a relaxation time of 5 min. The dense forcing is such that simulated and observed T - S and velocity profiles achieve a reasonable agreement just south of the reservoir at location T0 (Figs. 1, 2), which serves as a checkpoint to confirm the realism of the source water properties. Figure 2 indicates that an approximately 100-m-thick mixed bottom layer and much of the interfacial layer above are rendered well in the model [see Peters et al. (2005) for the vertical structure of the plume]. There is some disagreement between model and observations near 130-m depth, which is an effect of a counterflow generated in the model. The net barotropic flow is negligibly small in the model. Also the lateral boundaries are closed, and the strait is shallow and narrow. Thus, the baroclinic nature of the forcing leads to counterflows in the model solution. Nevertheless, it is not straightforward to impose open boundary conditions since entrainment (both vertical and lateral) implies that the overflow would not directly exit the domain, but water mass characteristics from outside of the computational domain need to be specified near the boundaries. Also, transport is conserved only globally and not necessarily in the regional sense; thus this issue also remains open to ad hoc approaches. Further impact resulting from the closed lateral boundaries on the model fields is minimized by terminating the experiments before outflow waters reach the vicinity of the boundaries. Their further spreading toward the Indian Ocean is therefore beyond our present scope. The initial condition for the stratification in the model domain outside of the northwest reservoir is set up by filling the interior with T - S profiles from a REDSOX station denoted T1 (Fig. 1) near the deepest part of the Tadjura Rift and outside of the overflow pathways. The profiles from this location are cropped vertically to match the depth at any other point.

Once the dense water mass starts flowing from the reservoir, the model is integrated for 20 days during which period the outflow reaches a quasi steady state

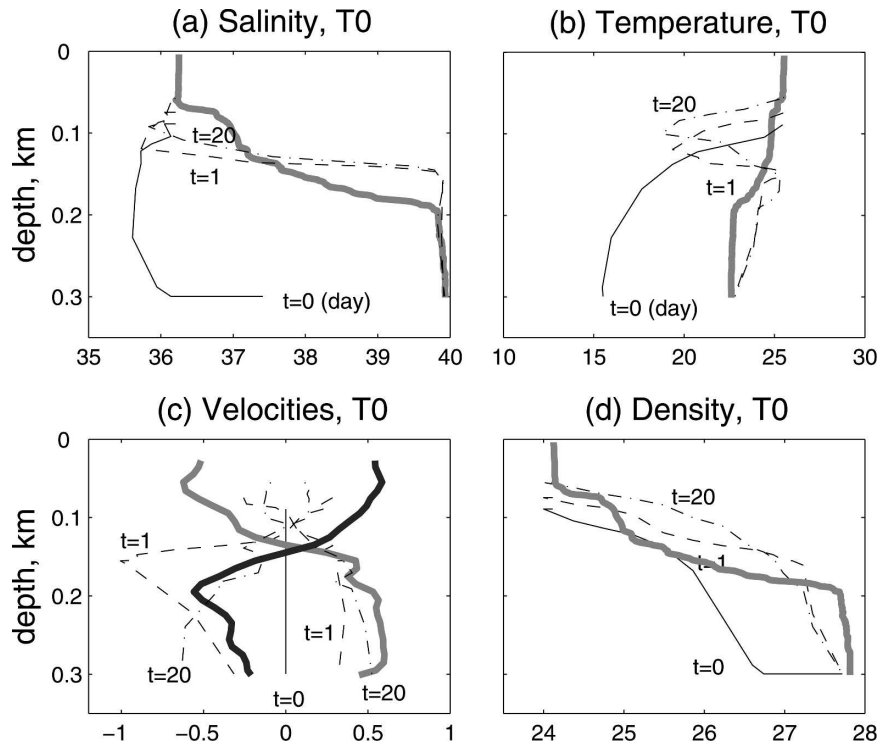


FIG. 2. Time evolution of (a) salinity (psu), (b) temperature ($^{\circ}\text{C}$), (c) velocity (m s^{-1}), and (d) density (σ_{θ}) profiles at station T0. Thick solid lines show the REDSOX profiles. Solid, dashed, and dashed-dotted lines show HYCOM profiles at 0, 1, and 20 days, respectively. In (c) the thick gray line shows u velocities (positive eastward) and the thick black line shows the v component (positive northward).

along the channels. Integration time steps vary from $\Delta t = 200$ s to $\Delta t = 50$ s depending on the horizontal grid size. The equation of state is approximated based on the work of Brydon et al. (1999). At a given reference pressure level, the density in sigma units is given by a seven-term polynomial function cubic in potential temperature and linear in salinity. One advantage of this simple representation is that it can be inverted to calculate any one thermodynamic variable when the others are given. Wind forcing as well as evaporation, precipitation, and radiative heat fluxes are set to zero everywhere by assuming that their net impact on the overflow is ultimately via the Red Sea circulation, which is represented by initializations from T0 and T1. It is also assumed that upper-ocean flows do not have a direct or significant influence on the overflow dynamics. Thus the boundary conditions for T , S , and velocity are those of no normal flux at the surface and the bottom. A quadratic bottom drag formulation with a drag coefficient of 3×10^{-3} is also used to represent the stress exerted by the bottom boundary layer on the overflow.

As for the vertical mixing parameterization, the entrainment formula developed by Xu et al. (2006) is em-

ployed for most of the simulations. This scheme is based on TP, which was developed by Hallberg (2000) specifically targeting overflow entrainment in isopycnic-coordinate models. Rather than an eddy diffusivity formulation, TP prescribes the entrainment velocity (ω_E) as a function of the local gradient Richardson number times the velocity difference between model layers (ΔU) of the form of an entrainment parameter $E = w_E/\Delta U = C_A f(\text{Ri})$. Chang et al. (2005) pointed out that this scheme allows for an adjustment of the flow to forcing through ΔU , which represents the shear between the layers resulting from differences in gravitational acceleration. In a set of numerical experiments with varying seafloor slopes, Chang et al. found that the entrainment parameter in TP increased in proportion to the slope angle. They concluded that TP has a promising structure for the parameterization of gravity currents. By comparing with nonhydrostatic, high-resolution, 3D model simulations, they proposed changes in the proportionality coefficient of C_A , while keeping $f(\text{Ri})$ identical to the one used by Hallberg (2000). On the basis of further numerical experiments and diagnostics, Xu et al. (2006) suggest a modification of $f(\text{Ri})$ as well, and propose a final formula:

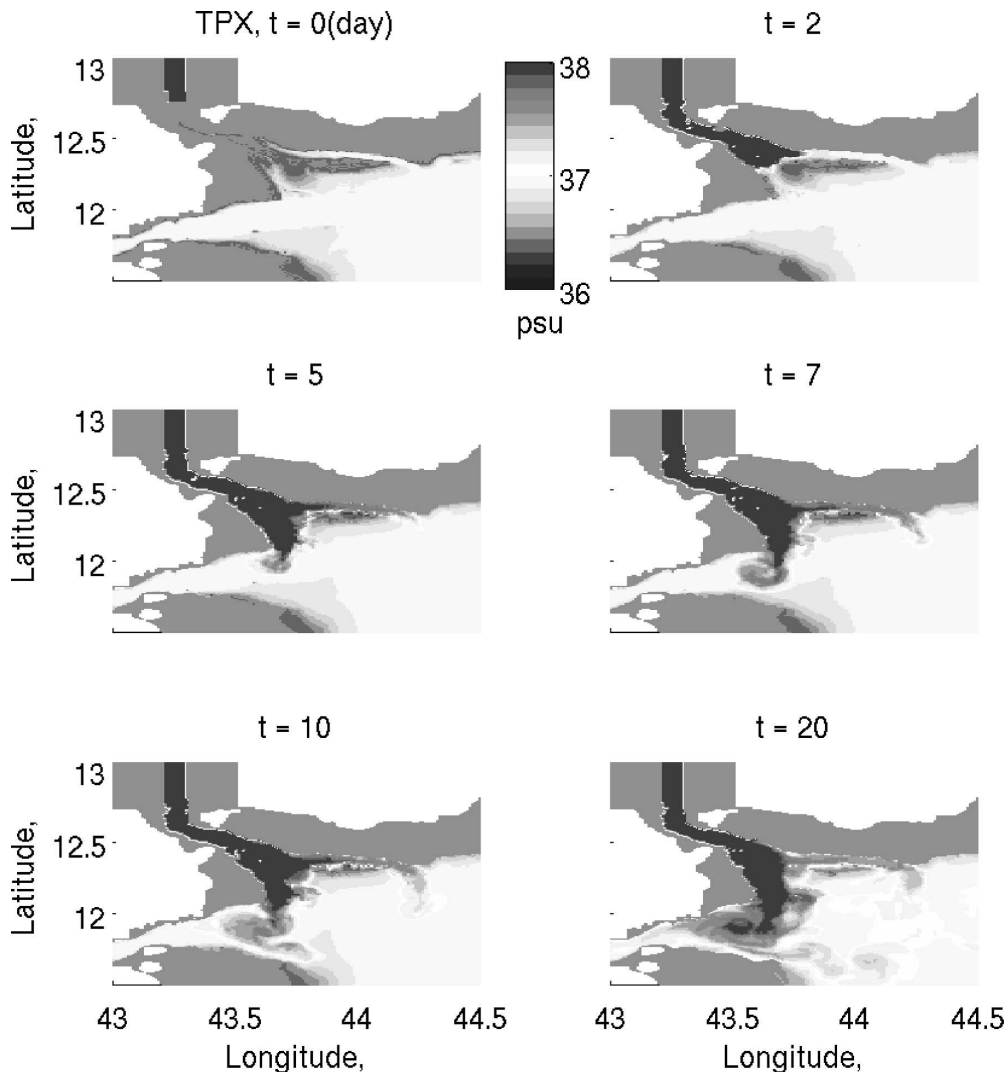


FIG. 3. Plan views of the time evolution ($t = 0, 2, 5, 7, 10,$ and 20 days) of the outflow propagation in terms of the salinity averaged over layers 10–14, which contain the overflow water masses.

$$E = \begin{cases} 0.2(1 - 4\text{Ri}) & \text{if } 0 \leq \text{Ri} < \frac{1}{4} \\ 0 & \text{if } \text{Ri} \geq \frac{1}{4}, \end{cases} \quad (1)$$

which is denoted as TPX here to differentiate from the previous versions. The reader is referred to Xu et al. (2006) for a detailed study on the development, testing, and comparison of TPX to other formulations. In particular, the use of TPX was shown to lead to accurate results in realistic simulations of the Mediterranean outflow in terms of the neutral buoyancy level and properties of product water masses. Thus, TPX is adopted as the main entrainment scheme in the Red Sea outflow computations herein. We also present and

evaluate results from KPP in the following (in section 4f).

4. Results

a. Initial propagation of the outflow

One of the research interests regarding outflows is the propagation pattern. In Fig. 3, model result of overflow propagation is shown in plan views of the salinity distribution at six different times during day 0 to 20. The overflows are visualized by averaging the salinity values in the 10th through 14th layers, which contain the overflow. Once the dense water in the reservoir is released, it takes not more than two days to reach the bifurcation point before it separates into the two chan-

nels. After the bifurcation, the speed of propagation becomes slightly lower as it takes five days for the two branches of outflow to reach the Tadjura Rift. Note that both channels are fully occupied with the overflow water masses after approximately five days. (The change of the propagation speed can also be clearly seen in Fig. 5, in which the propagation speed is reduced after the overflow passes the bifurcation point located at a distance of approximately 60 km from Bab el Mandeb Strait.) Upon reaching the Tadjura Rift, the outflows are no longer constrained by the channel topography and start mixing laterally as well. In particular, it is clear from Fig. 3 that the two branches of the overflow, which were split downstream of Bab el Mandeb Strait, interact again along the Tadjura Rift. The significance of this observation is that the water masses released from the southern channel may impact the equilibrium level of those coming from the northern channel. In this way, the Red Sea overflow may differ from the more comprehensively studied Mediterranean and Denmark Strait overflows. Nevertheless, integrations are terminated at $t = 20$ days, given closed domain boundaries (as discussed above) that prohibit an adequate investigation of this issue. Longer-term and larger-scale simulations of this problem may be of interest regarding the circulation in the Gulf of Aden and also in the Indian Ocean. However, a closer investigation of this process is out of the scope of the present study.

The propagation of the outflow is also investigated using the profile views of the salinity distribution along the two channels (Fig. 4). To investigate the propagation more closely, five time steps are chosen from $t = 1$ to 9 days by 2-day intervals. Even before day 1 passes, the dense water rapidly fills the channel up to 400 m where a flat basin is located near the bifurcation point ($x \approx 20 \sim 55$ km). After the outflow passes this point, the propagation speed and overflow transport decreases. The dense overflow constantly propagates down along the northern channel until it reaches the Tadjura Rift ($t = 3, 5,$ and 7 days). Then, the overflow starts to detach from the bottom and penetrate into the interior within an equilibrium depth range. In the case of the southern channel, it takes less time to reach the Tadjura Rift because of the shorter distance from the bifurcation point. In this case, it is easier to notice the process of entrainment with ambient flows from the gradual increase in the thickness of the overflow ($x > 50$ km).

It is not possible to directly compare the initial propagation speed with that from the observations because the REDSOX data represent a snapshot of the fully developed outflow plume. However, an approxi-

mate calculation can be made by estimating a propagation speed based on the interfacial wave speed. Under the assumption of a two-layer system at Bab el Mandeb Strait, the initial propagation speed of a gravity current, U_F , can be estimated from

$$U_F = \sqrt{\frac{g'h_1h_2}{(h_1 + h_2)}}, \quad (2)$$

where $g' = g(\beta\Delta S - \alpha\Delta T)$ is the reduced gravity with $\Delta S \approx 3$ psu, $\Delta T \approx 7^\circ\text{C}$, $\alpha \approx 2 \times 10^{-4} \text{ }^\circ\text{C}^{-1}$, $\beta \approx 7 \times 10^{-4} \text{ psu}^{-1}$, and the thickness of outflow, $h_1 \approx h_2 \approx 150$ m from Fig. 2. According to this simple analysis, the propagation speed becomes $U_F \approx 0.7 \text{ m s}^{-1}$, consistent with an average speed that can be estimated from the REDSOX velocity profiles (presented in Fig. 11). However, this is also much larger than the average speed of initial propagation of the modeled overflow, which is approximately 0.3 m s^{-1} , and demands an explanation.

Three possible hypotheses are put forth to explain this discrepancy: 1) The propagation is slower due to the friction and stress exerted by the development of bottom and lateral boundary layers within the narrow channels. 2) It is due to the small average channel slope of about 0.33° in the northern channel and given that the bottom drag is found to play an increasingly important role in gravity currents as the slope becomes flatter (Britter and Linden 1980). 3) It is due to the rough bottom topography along the two channels (e.g., Fig. 4).

The first and second hypotheses are tested by performing several simulations using idealized channel geometry with bottom slopes varying from 0.33° to 3.0° . Also, the effects of lateral boundaries are examined by imposing no-slip boundary conditions at the sidewalls. The result is then compared with that of gravity currents generated by imposing a free-slip lateral boundary condition. It is found that the lateral boundary conditions as well as the small channel slopes do not significantly change the speed of propagation because their effect does not exceed 10% when compared to one another. Other conditions such as channel width (varied from 5 to 10 km) and horizontal grid spacings (varied from 0.1 to 1 km) are also not found to cause a significant difference in the outflow propagation speed.

The third hypothesis is examined by calculating the initial propagation (head) speed of the computed gravity currents. The speed of the outflow head is expressed as a function of the position along the northern channel in Fig. 5a where the propagation speed, U_F , is plotted as a function of distance. Apparently, the initial propagation speed is not uniform in time, but is reduced once the overflow passes over the bifurcating point ($x \approx 55$

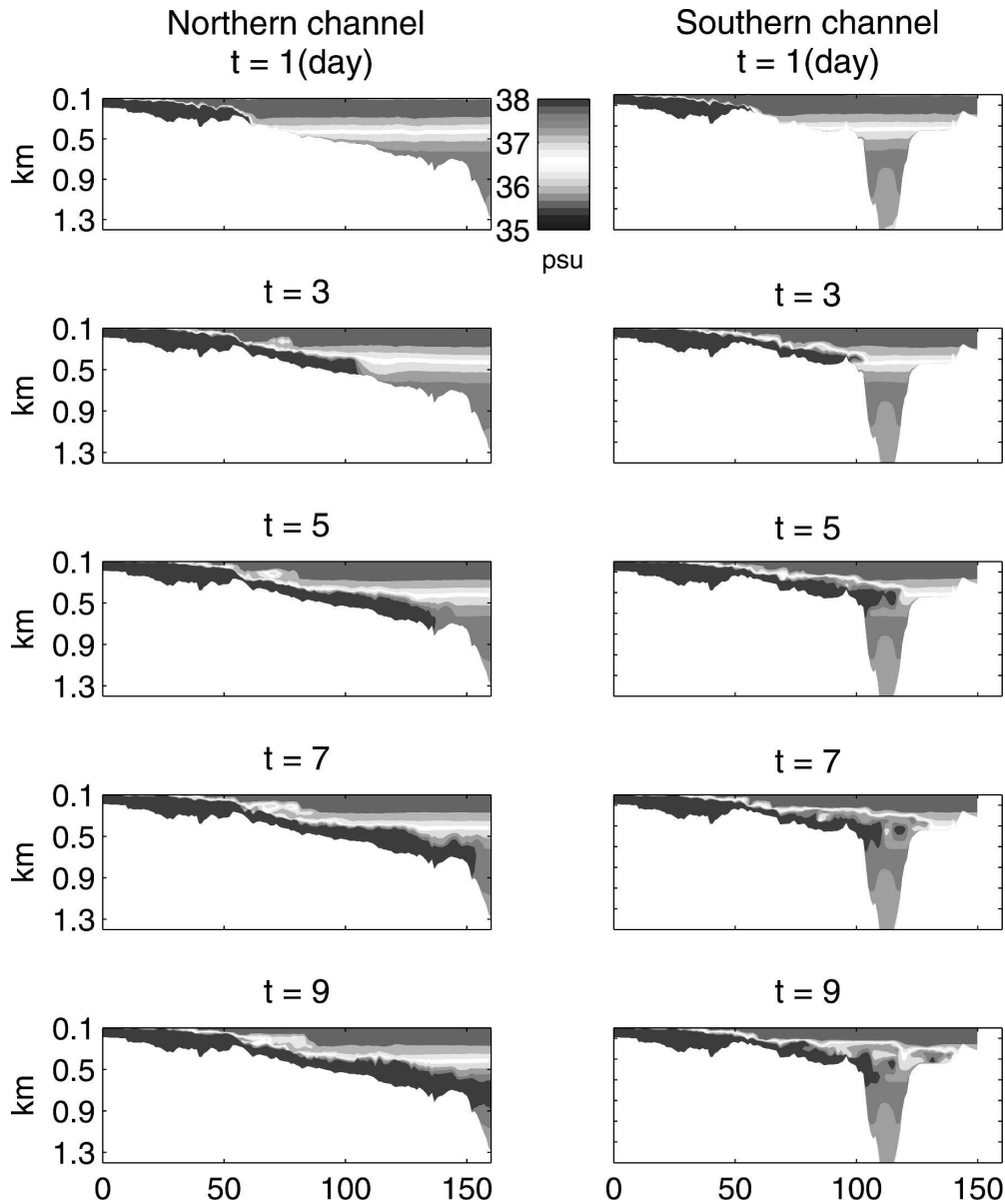


FIG. 4. Profile views of the time evolution ($t = 1, 3, 5, 7,$ and 9 days) of the overflow salinity distribution along the (left) northern channel and (right) southern channel. The distance starts from the southern exit of Bab el Mandeb Strait.

km). In addition to this variability of the initial propagation speed near the bifurcating point, Fig. 5a also indicates that there are locations that lead to a dramatic reduction in the speed at $x \approx 30, 43, 53, 62, 70, 83$ km. These locations correspond to those of large bumps in the bottom topography (Fig. 5b). Except for these bumpy locations, U_F recovers the estimated speed [from (2)] of approximately 0.7 m s^{-1} . Therefore, we conclude that the nonuniform propagation speed of computed Red Sea outflows is caused by the bumpy topography along the channel, which significantly re-

duces the anticipated propagation speed of the initial density front.

b. Comparison of modeled and observed temperature and salinity profiles

The salinity (S) profiles are compared with the REDSOX observations at several locations along the two channels. Eight locations are chosen along the channels to compare the vertical distributions of T - S profiles with the model output (Fig. 1). Five locations are chosen in the northern channel (N1 to N5) and

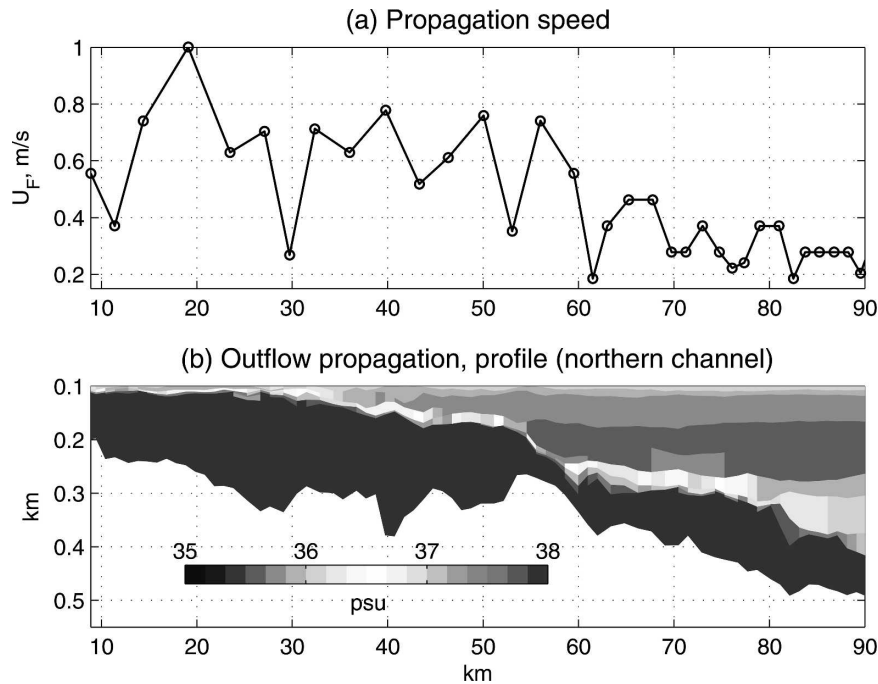


FIG. 5. (a) Initial propagation speed of the modeled overflow and (b) section of bottom topography along the northern channel. Note that the propagation speed is significantly reduced at locations where rough bottom topography is encountered.

three in the southern channel (S1 to S3). The salinity profiles are compared for the 1-km horizontal resolution case in Fig. 6. In this figure, the measured salinity is compared with time mean distributions of computed profiles. The time interval chosen for averaging is from day 10 to 20, after the outflow reaches a quasi steady state and shows little variation in the computed profiles. To show the variability of the profiles during this time period, 95% confidence intervals are shown as envelopes around the mean profiles. Also, the initial profiles ($t = 0$) are plotted to show the difference from the computed Red Sea overflows at each location. The computed profiles exhibit large differences from the observed profiles at $t = 0$ because the dense current has not reached these points yet. The discrepancy is greatly reduced after the outflow passes each location, ultimately achieving reasonable agreement with the observations. A nice match is especially found close to the bottom where the dense water mass is located. Although the agreement is satisfactory, especially at N2, N3, and N4 where the outflow mass is concentrated within the narrow northern channel, some disagreements are found at N1, S1, and S2 because a high salinity water mass is observed near the elevation of $z = 100 \sim 200$ m, namely, higher up in the water column. It is thought that the formation of this water mass is related to mixing processes taking place within Bab el

Mandeb Strait (Matt 2004) and such mixing could be induced by tidal forcing, which is most pronounced in this strait because of its shallow depth and narrow geometry. However, tidal forcing is not included in the present model.

In Figs. 7 and 8, modeled along-channel salinity profiles are compared with REDSOX observations from the northern and southern channels, respectively. The modeled salinity distributions are plotted at every grid point along the individual channels at $t = 20$ days. For the observations, the distributions are obtained by interpolating between the vertical profiles measured at the (9 and 5, respectively) stations in the northern and southern channels. Because of the subsampling in space along the channels, the observed distributions do not contain as much detailed information as those from the model. The contours along the northern channel generally show reasonable agreement with the observations. For $x > 100$ km, the thickness of the computed overflow increases and becomes comparable with the observation. Also, it is noticed that both contours have gradation in salinity level, which shows evidence of entrainment with ambient flows in these areas. Along the southern channel (Fig. 8) where the observed contours are rough due to an even smaller number of measurement locations, the entrainment is even more clearly seen at $x > 70$ km in the computed overflow. Given the

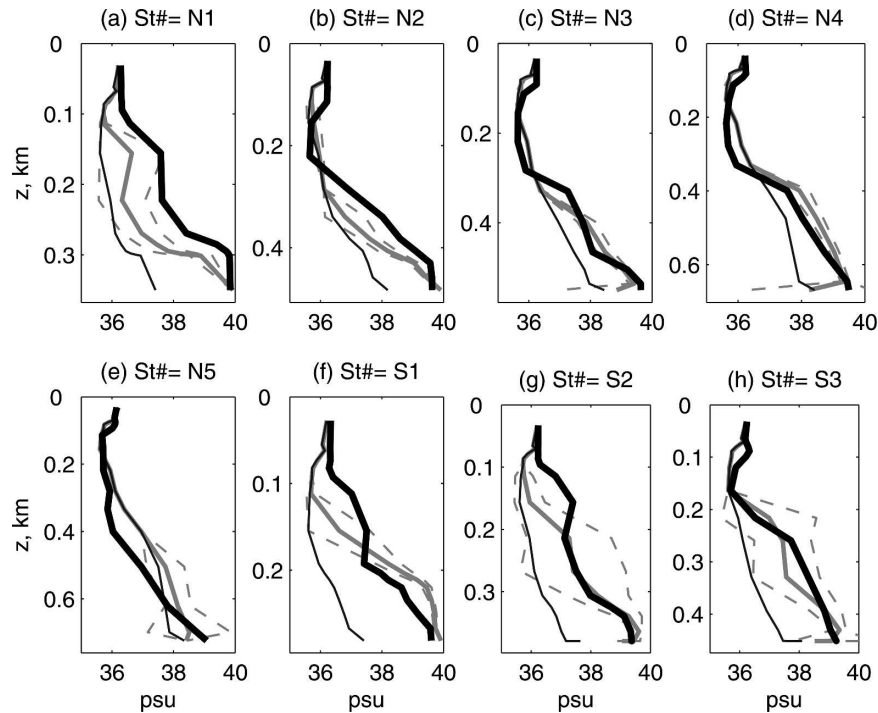


FIG. 6. Comparison of salinity profiles in the northern channel (N1–N5) and southern channel (S1–S3) stations. Thick black solid lines: REDSOX profiles vertically averaged to obtain mean values corresponding to the 16 layers in HYCOM. Thick gray solid lines: HYCOM profiles (TPX, $\Delta x = \Delta y = 1$ km) time averaged from day 10 to 20. Dashed/gray lines: 95% confidence intervals of computed profiles indicating time variability. Narrow black solid line: model initialization from T1 (note that the water depth is different at the station location but the initialization profiles are identical at the same level).

three-dimensional nature and possible time variability of the flow field, comparison of snapshots along two-dimensional sections can only provide incomplete insight on the degrees of freedom and model realism. Nevertheless, this is the extent of comparison that can be carried out given the REDSOX observational dataset at the present time.

Cross-sectional views of the overflows are also compared with the observations using the salinity distributions along sections 1 to 3, which cross the two channels at three different distances from the source location (Fig. 1). The salinity profiles from REDSOX stations along each channel section are interpolated and shown in comparison to HYCOM salinity distributions in Fig. 9. The areas occupied by salty water masses are reasonably well reproduced by the model. The largest discrepancy between the modeled and observed salinity distributions is found in the upper ocean above the southern channel at sections 1 and 2. Again, this water mass is likely to be caused by mixing processes inside Bab el Mandeb Strait, which are not represented in this model. There are also differences regarding the distri-

bution in maximum salinity near the bottom of the northern channel at section 3 as well.

We also briefly present a comparison of the product water masses from the two channels to those from the observations. Figure 10 shows cross-sectional views of the salinity distributions along sections 4 and 5 (Fig. 1) where the overflows leave the two channels and reach neutral equilibrium in the Tadjura Rift. Several interesting observations can be made on the basis of Fig. 10. The traditional view based on so-called stream-tube models of overflows (e.g., Killworth 1977; Baringer and Price 1997a; Bower et al. 2000) is that the product water mass is a coherent structure consisting of a single density. We note from Fig. 10 that the modeled product water masses do not consist of a single core, but the outflow from the northern channel equilibrates at two density layers, whereas the outflow from the southern channels equilibrates at three density layers. Furthermore, the two channels lead to product water masses that equilibrate at a different range of densities from each other. Thus, the depths of the salinity maxima from both channels are slightly different. The northern

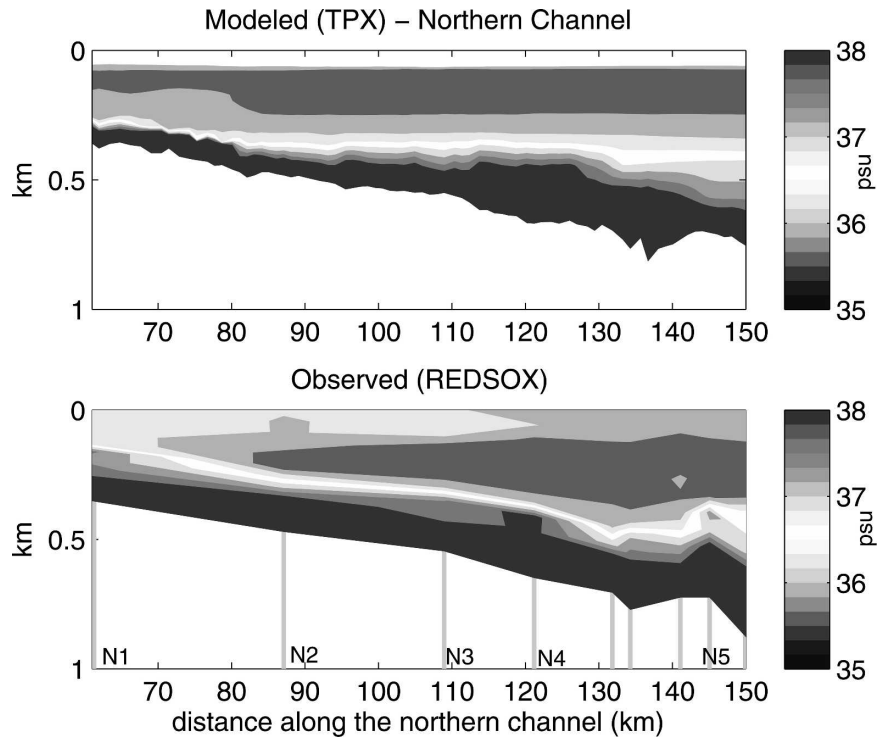


FIG. 7. Comparison of salinity distributions along the northern channel from (top) the HYCOM simulation and (bottom) REDSOX observations. In the bottom panel, the continuous distribution is obtained by interpolating REDSOX profiles from nine stations marked by the gray lines.

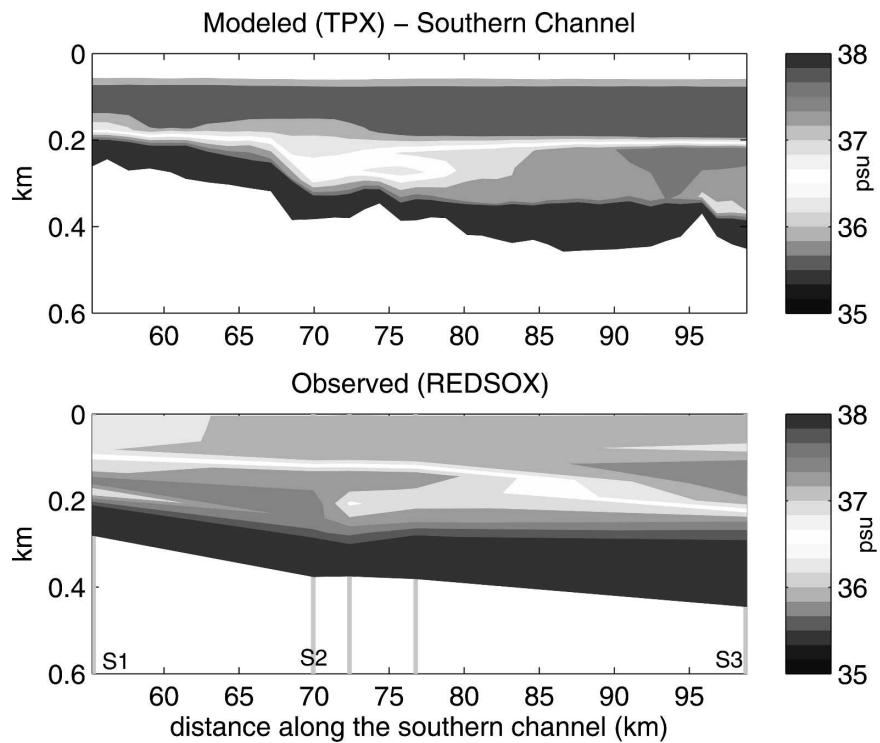


FIG. 8. As in Fig. 7, but for the southern channel.

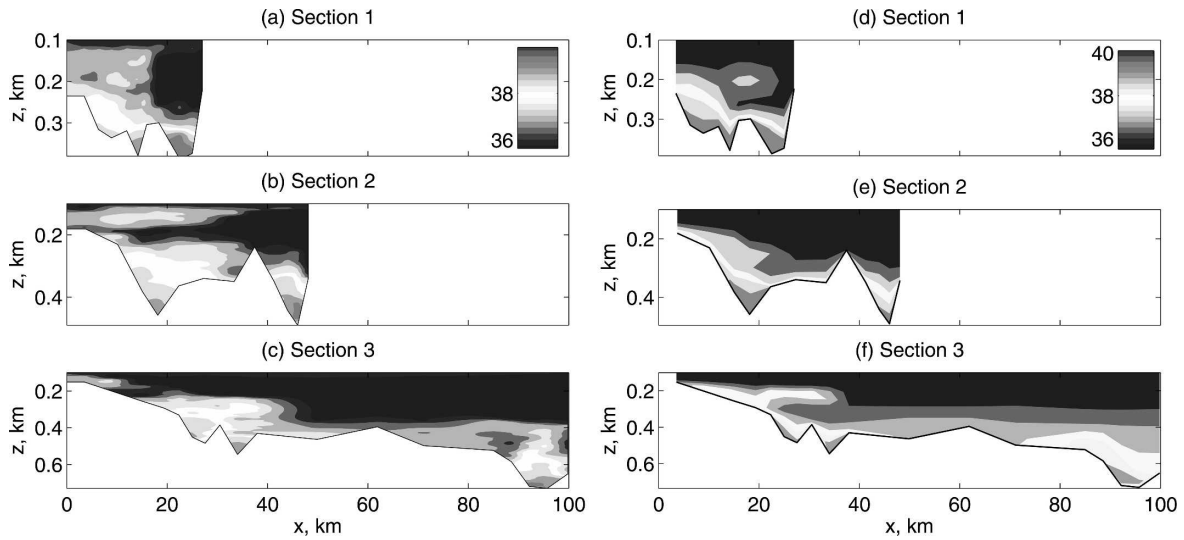


FIG. 9. Salinity distributions across the outflow plume from REDSOX at (a) section 1, (b) section 2, and (c) section 3 and from HYCOM at (d) section 1, (e) section 2, and (f) section 3.

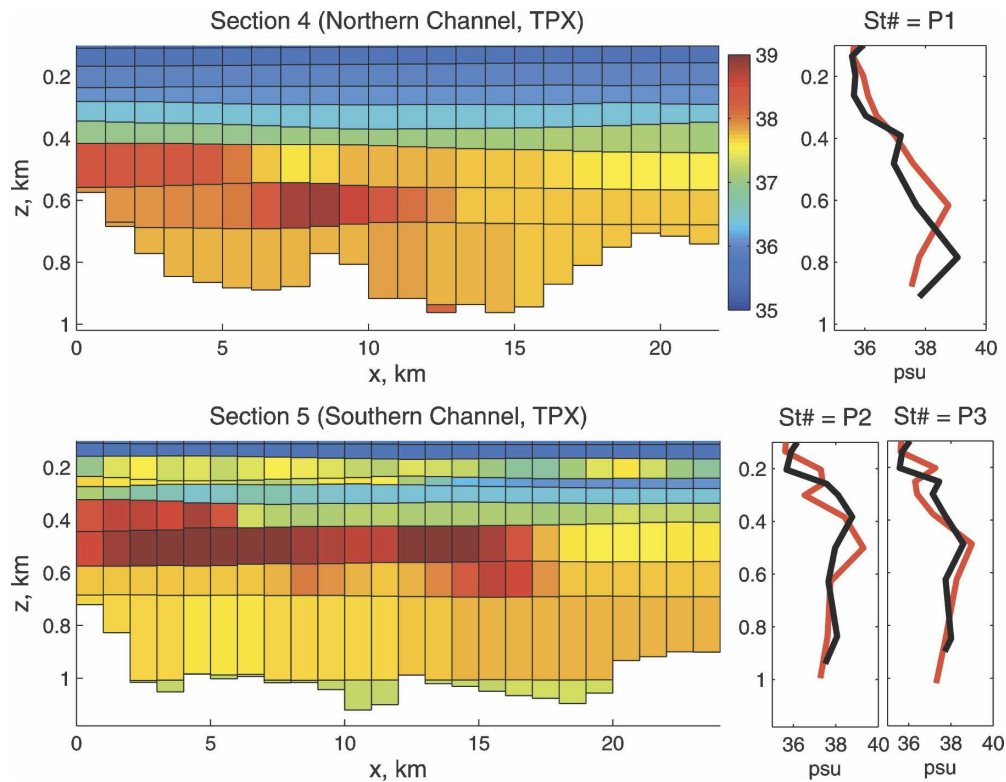


FIG. 10. Salinity distributions along sections crossing the northern (section 4) and the southern channel (section 5) at the interface with the Tadjura Rift. Also, the comparison of salinity profiles at stations P1, P2, and P3 between observed (black lines) and computed (red lines) profiles. Refer to Fig. 1 for locations of section 4, section 5, P1, P2, and P3. The horizontal size of the cells corresponds to the horizontal grid spacing (1 km) and the vertical size to the layer thickness. The layers also indicate the density classes.

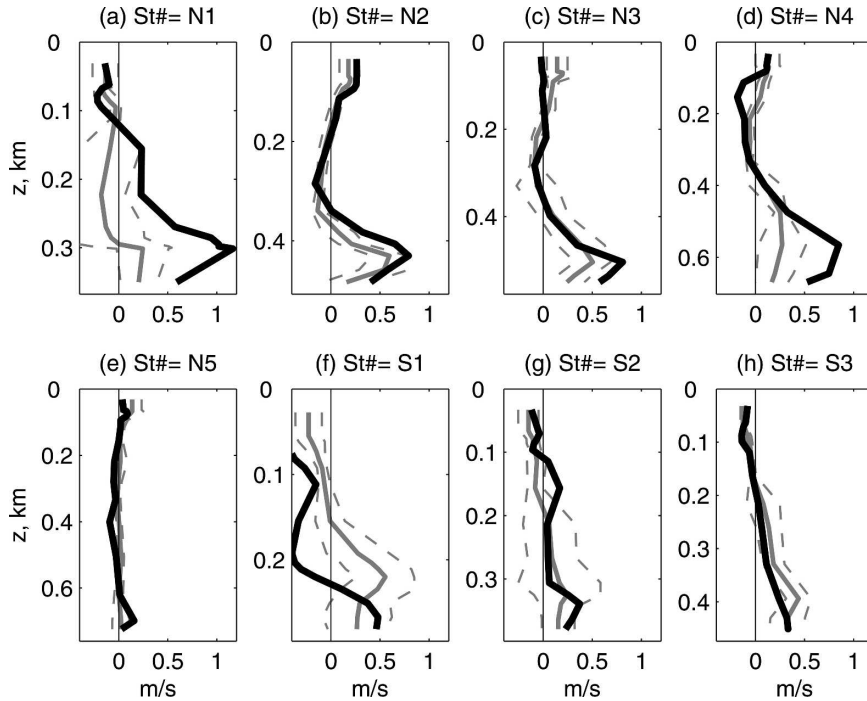


FIG. 11. Comparison of the streamwise velocity profiles in the northern channel (N1–N5) and southern channel (S1–S3) stations. Black solid lines: REDSOX profiles vertically averaged to obtain mean values corresponding to the 16 layers in HYCOM. Gray solid lines: HYCOM profiles (TPX, $\Delta x = \Delta y = 1$ km) time averaged from day 10 to 20. Dashed lines: 95% confidence intervals of computed profiles indicating time variability. Thin black line: model initialization.

channel has its salinity maximum at $z \sim 0.65$ km while the maximum is about $z \sim 0.55$ km for the southern channel. Comparison to observations is shown at station P1, which is near the middle of the northern channel exit, and at stations P2 and P3, which captures the main two branches of the southern channel overflow (Fig. 1). There is reasonable agreement between the model results and observations. A closer look indicates that the depth of maximum salinity of the observed profile in P1 ($z \sim 0.8$ km) is greater than that obtained from the simulation ($z \sim 0.6$ km), which could be because the model does not transport accurately the densest bottom layers along the northern channel (Fig. 6). However, it is not known how well station P1 represents the overflow plume along section 4. In contrast, the salinity maximum is less deep in the model than in the observations at station P2. The agreement is quite satisfactory for station P3. Overall, the comparison of equilibrated product water masses appears to be a demanding test for model fidelity. It is also of interest to explore the interaction between the overflow water masses produced from the two channels. These challenging problems will be pursued further in a future study.

c. Comparison of modeled and observed velocity profiles

The modeled velocity profiles are compared with the observations at eight selected locations in the northern (N1 to N5) and southern (S1 to S3) channels (Fig. 11). The two velocity components, u and v , are projected along the flow direction so that just the velocity magnitude can be compared. In the same way as the T – S profiles shown in Figs. 6 and 7, the simulated velocities are averaged over days 10 to 20 with the envelope of 95% confidence intervals. The observed profiles are vertically averaged to match the model discretization within each model layer.

Reasonable agreement with REDSOX observations can be found at some locations, such as stations N2 and N3. The magnitude of modeled velocity profiles is typically less than those from observed profiles at the other locations of the northern channel, namely, at N1, N4, and N5. This underestimation seems to increase in proportion to the distance from the Bab el Mandeb Strait. The maximum velocity magnitude of the averaged simulated profile at location N4 is about 35% of that of the observed profile. In particular, it is not clear what

happens to the overflow at station N5, which shows a significant reduction in the peak speed. We note however (Fig. 1) that N5 is where the channel width starts to widen such that it is desirable to compare velocities across the entire channel section rather than at a single profile.

Mismatches in the velocity profiles appear less pronounced in the case of the southern channel. At S1, the magnitude becomes comparable with the observation, although the thickness of the simulated dense overflow is larger than the observations. In S2 and S3 the discrepancy is reduced, and good agreement is found between the two profiles with both indicating maximum downstream velocities of about 0.4 m s^{-1} .

It appears that the southern channel velocity distributions are somewhat overestimated, whereas those in the northern channel are underestimated in the model with respect to those from the observations. Thus, factors controlling the bifurcation of the outflow into the southern and northern channels may have an effect on the velocity distributions. These factors include the accuracy of the bottom topography, hydraulic control, time dependence (inherent and that due to forcing) in the outflow, all of which require either higher model and data resolution and/or more comprehensive forcing that is missing in the present study.

d. Comparison of modeled and observed volume transport

The volume transport of the outflow, $Q = \int_A \mathbf{u} \cdot d\mathbf{A}$, where A is the cross-sectional area of the overflow, is estimated as a function of time at the three sections shown in Fig. 1. These sections are chosen to coincide with the observational data, as reported by Matt and Johns (2007). In the calculation of Q , the velocity vectors are projected along the flow direction at each grid point for the sections. Following Matt and Johns (2007) a lower limit of salinity of 36.5 psu defines the top of the overflow. In addition, we check whether all flows below the 36.5-psu pycnocline are along the streamwise direction, and exclude counter flows in the calculation of the transport. An example of the calculated transport Q is given in Fig. 12, which shows the 10 km of cross-sectional view of the northern channel at N3. All of the grid points in this area are expressed in their actual size after they are averaged over days 16 to 20. The averaged salinity level of each grid point is contoured in the range of 35 to 40 psu. Also, streamwise velocities are calculated over each model cell, defined by the layer thickness in the overflow and the horizontal grid spacing. Then, Q is calculated by integrating the product of the area and velocity of every computational cell that belongs to the overflow at sections 1, 2, and 3. Despite

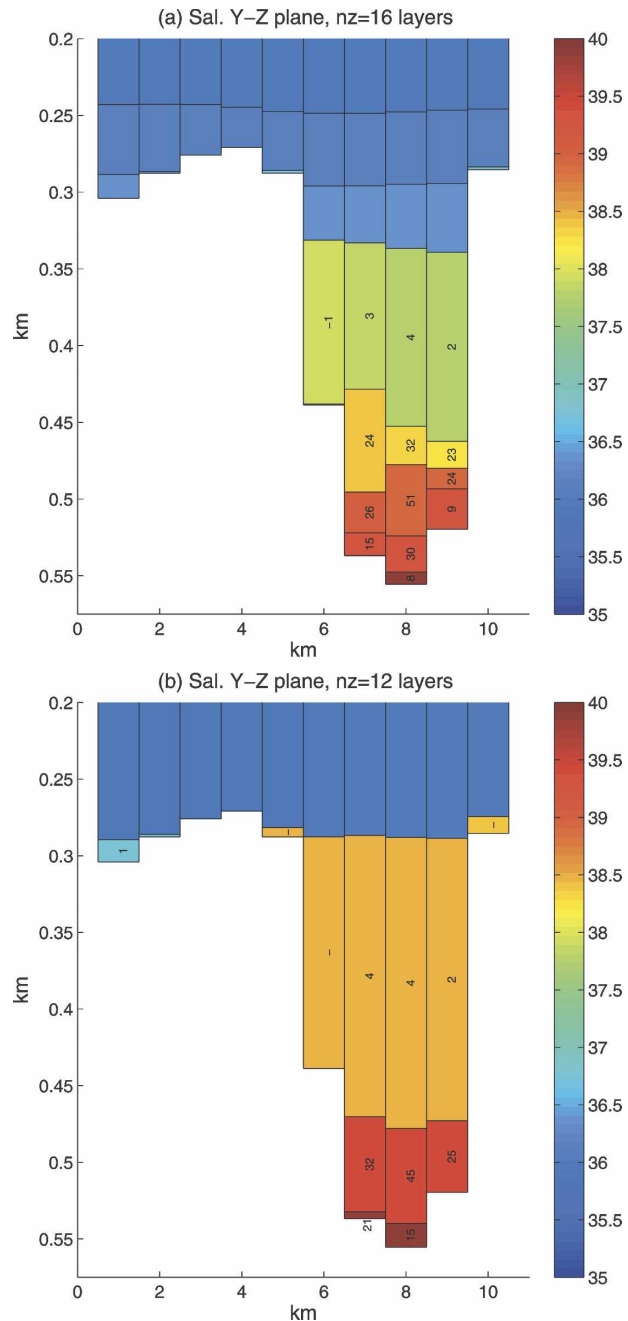


FIG. 12. Cross-sectional view of the salinity distributions at each cross-sectional cell crossing the northern channel at station N3 and $t = 20$ days from (top) the standard model experiment with 16 layers and (bottom) an experiment with 12 layers. The superimposed numbers denote the streamwise velocity magnitude in each cell (cm s^{-1} , positive streamwise).

the Lagrangian nature of the vertical coordinate system, which facilitates the resolution of high density gradient regimes that tend to coincide with locations of high entrainment in overflows, it is found that a certain number of layers is necessary in order to adequately

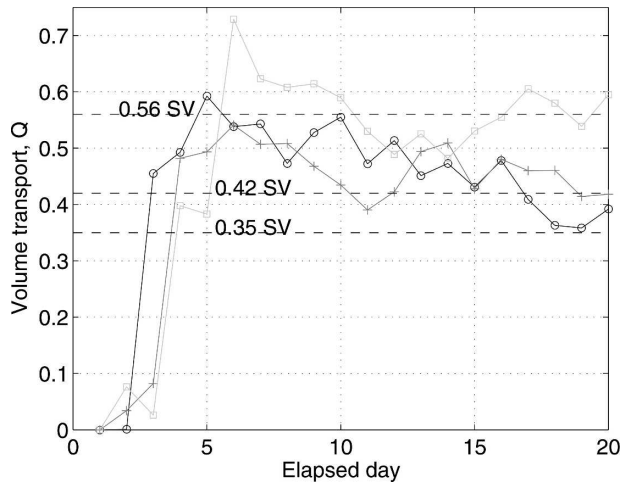


FIG. 13. Volume transport Q of the Red Sea outflows at sections 1 (gray crosses), 2 (black circles), and 3 (gray squares) in comparison with those estimated from REDSOX observations (dashed), which are 0.35 Sv (section 1), 0.42 Sv (section 2), and 0.56 Sv (section 3).

capture the overflow structure, and particularly the transport, accurately. We find that the transports become inaccurate when 12 layers (instead of 16) are used, because the overflow salinity and velocity structure are not well resolved in this case (Fig. 12). It appears 16 layers correspond to an optimal choice for this study considering a balance between increasing computational cost and diminishing improvement in accuracy when a larger number of layers are used.

Figure 13 shows the comparison between the modeled results and the observed volume transport. The observations show that, as a result of entrainment, Q increases with distance from the Bab el Mandeb Strait, namely, from 0.35 Sv ($\text{Sv} \equiv 10^6 \text{ m}^3 \text{ s}^{-1}$) at section 1 to 0.42 Sv at section 2 and to 0.56 Sv at section 3. It should be noted that the observations are based on quasi-synoptic single time sampling at these locations. Also, a cross-sectional extrapolation of the velocity and salinity data from individual stations was carried out in order to estimate Q from observations (Matt and Johns 2007). Therefore, it is not clear to what extent one should seek agreement between model and REDSOX transports. The simulated results as well as the observed velocities (Peters et al. 2005) show strong variability in time and thus pose a challenge in estimating reliable mean values for model–observation comparison. At all sections the transport has maximum values just after the overflow passes each section, which may be due to the formation of a head at the leading edge of the overflow. After the passage of the leading edge of the overflow, the transport rate is gradually reduced. In case of section 1, this gradual reduction continues until day 20. In sections 2

and 3, however, the transport rate stops decreasing after day 12 and tends to be stable within a high range of variability.

Consistent with the observations, the simulated transport rate increases with the distance from the Bab el Mandeb Strait, a result of the entrainment of ambient fluid. In section 4c, it was shown that the velocity magnitude decreases with distance from the Bab el Mandeb Strait along the northern channel. However, it turns out that the velocity underestimation does not severely affect the total transport rate as Q keeps increasing with the distance. This is because the area of the overflow increases as well. The simulated result shows that the transport of the dense overflow inside the northern channel increases by about a factor of 1.5 from N2 to N4. Matt and Johns (2007) do not estimate the overflow transport in the northern and southern channels separately, but based on a two-dimensional nonhydrostatic model computation, Özgökmen et al. (2003) find an increase of approximately 1.6-fold in the northern channel, consistent with the HYCOM simulation.

The direct comparison of modeled and observed transports across individual sections has to be taken with a grain of salt because the model and observations show high levels of variability. Nevertheless, the modeled transport rates tend to become stable after day 12 for sections 2 and 3. So, if averages are taken for each section from day 12 to day 20, one gets 0.41 Sv, 0.44 Sv, and 0.55 Sv for sections 1, 2, and 3, respectively, in approximate agreement with those estimated from REDSOX data.

e. Sensitivity to horizontal grid spacing

Section 4a shows that the seabed topography is an important factor that affects the overflow propagation significantly. Therefore, the horizontal grid size may be an important issue as well because it determines the resolution of the narrow channels inside of which the main body of the overflows are confined, and all other fine details of topography. In addition, the Ri dependence of Eq. (1) raises the question of how the performance of the entrainment parameterization changes with grid spacing. This issue was previously investigated by Chang et al. (2005) in an idealized setting with the conclusion of low sensitivity, but not in a realistic overflow simulation.

To examine the sensitivity of the results to the grid size, plan views of the simulated outflow are compared between different horizontal grid sizes, namely, for $\Delta x = \Delta y = 0.5; 1; 2;$ and 5 km (Fig. 14). As long as the grid size does not exceed 2 km, the bifurcation of the outflow into the two channels, as seen in the observation, can be captured by the model. If the grid size is

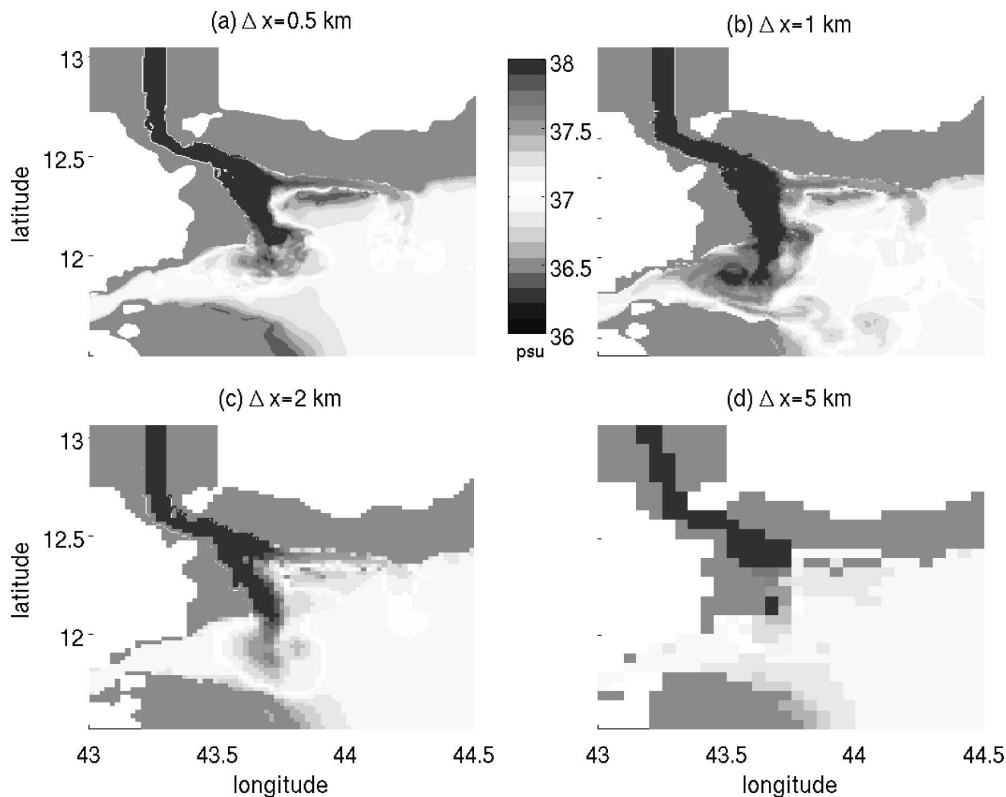


FIG. 14. Outflow patterns resulting from different grid sizes, as depicted using the salinity distribution in layer 10 and at $t = 20$ days: (a) $\Delta x = 0.5$ km, (b) $\Delta x = 1$ km, (c) $\Delta x = 2$ km, (d) $\Delta x = 5$ km.

increased to 5 km, however, the outflow pattern is grossly misrepresented in the model. In this case, the dense flows along the northern channel disappear and the flows are blocked even in the southern channel. This large discrepancy results from the failure of the coarse grids to capture the narrow channels. Finally, we note that the relative partitioning of the overflow between southern and northern channels is very sensitive to the horizontal grid spacing as well. In particular, the preferred behavior in coarse-resolution cases is to flow into the southern channel, because it is a more direct pathway, while diversion of part of the overflow into the northern channel requires more precise resolution and dynamics.

A more detailed comparison is shown for salinity profiles computed from $\Delta x = \Delta y = 0.5$ km and $\Delta x = \Delta y = 1$ km (Fig. 15). It appears that the two different horizontal resolutions generally generate consistent results, having small differences from each other. Therefore, the variation in grid resolution may not greatly affect the results as long as it is fine enough to resolve the channels. Results from $\Delta x = \Delta y = 2$ km and $\Delta x = \Delta y = 5$ km are not plotted because the locations of the stations are not accurate in these cases.

In light of such significant dependence of topographic details to grid spacing, the sensitivity of the performance of Eq. (1) clearly becomes a secondary consideration. Specifically, if the geometry is not accurate enough to represent the main flow pathways, the dynamics are already considerably modified, and one cannot expect a mixing parameterization to rectify the computation.

f. Effect of different entrainment schemes

As investigated in sections 4a and 4e, the seabed bottom topography and the horizontal grid resolution are the factors that most significantly affect the model simulation results. These geometric factors are important because the main pathways of the Red Sea overflows are characterized by relatively smaller scales compared to other overflows such as the Mediterranean overflow or the Denmark Strait overflow. Also, the large-scale slope of the bottom topography is about $1/3^\circ$, which is two- to threefold smaller than those in the other overflows mentioned above. Therefore, the vertical mixing schemes that played an important role in those overflows may act differently in the Red Sea overflow. To investigate the impact of the vertical mixing in

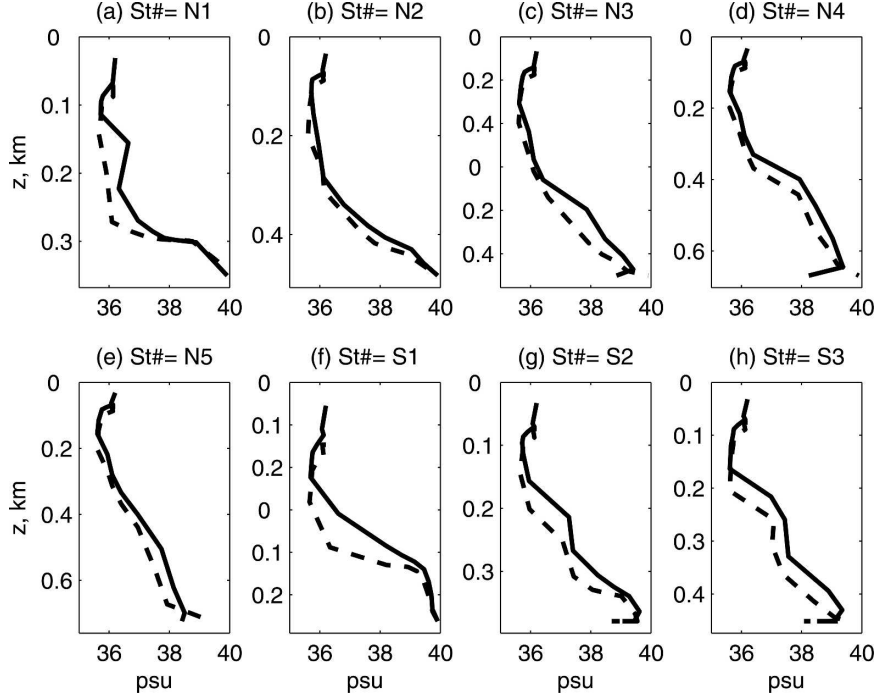


FIG. 15. Comparison of salinity profiles from different horizontal grid spacings, $\Delta x = 1$ km (solid) and $\Delta x = 0.5$ km (dashed).

the isopycnal coordinate model employed herein, KPP, a popular scheme used in many OGCMs is used in addition to the main scheme TPX.

The KPP scheme has a number of components addressing different physical processes. Of these, only the parameterization of shear-driven mixing in the form of eddy viscosity and eddy diffusivity as functions of the local gradient Richardson number is relevant for this study. The gradient Richardson number Ri is the ratio of the squared buoyancy frequency N^2 and the squared vertical shear,

$$Ri = N^2 \left[\left(\frac{\partial u}{\partial z} \right)^2 + \left(\frac{\partial v}{\partial z} \right)^2 \right]^{-1}.$$

The vertical eddy diffusivity is given by

$$K_{\text{shear}} = K_{\text{max}} \times \left[1 - \min \left(1, \left(\frac{Ri}{Ri_c} \right)^2 \right) \right]^3 \quad (3)$$

so that vertical diffusivity is zero when $Ri \geq Ri_c$ with $Ri_c = 0.7$. When $Ri < Ri_c$, vertical diffusivity gradually increases to account for stronger mixing due to weaker stratification, and at the limit of $Ri = 0$ mixing takes place with an intensity qualified by K_{max} . Large (1998) estimated the value of K_{max} from large-eddy simulations of the upper equatorial Pacific, specifically finding $K_{\text{max}} = 50 \text{ cm}^2 \text{ s}^{-1}$.

In Fig. 16 the propagation patterns resulting from

KPP and TPX are compared in terms of plan view (top panels) as well as the profile view (bottom panels) of the salinity distribution at day 10. Clearly, both schemes yield very similar patterns of the modeled overflows. The propagation pattern differs slightly once the dense flows arrive at the Tadjura Rift and start reaching neutral buoyancy while spreading horizontally by lateral mixing as well. The similarity between the two mixing schemes is also confirmed using profile views. The thicknesses of the overflows are almost same at every location along the channel and show no significant difference between the two schemes.

To quantify the difference between the results of the two schemes, an error function is used by normalizing the deviation of the simulated salinity profiles from the observations as

$$\text{err}^i(t) = \frac{\sqrt{\sum_{j=1}^{j=N^i} [\bar{S}r_{\text{model}}^i(j) - Sr_{\text{obs}}^i(j)]^2 / N^i}}{\Delta Sr}, \quad (4)$$

where $\bar{S}r_{\text{model}}^i$ is the time-averaged model output of tracer (salinity) and Sr_{obs}^i is the observed value at station i , N^i is the number of sampling points, and $\text{err}^i(t)$ is the rms error normalized by tracer ranges ΔSr ($\Delta S = 4.3 \text{ psu}$, $\Delta T = 11^\circ\text{C}$). In Fig. 17 the error function,

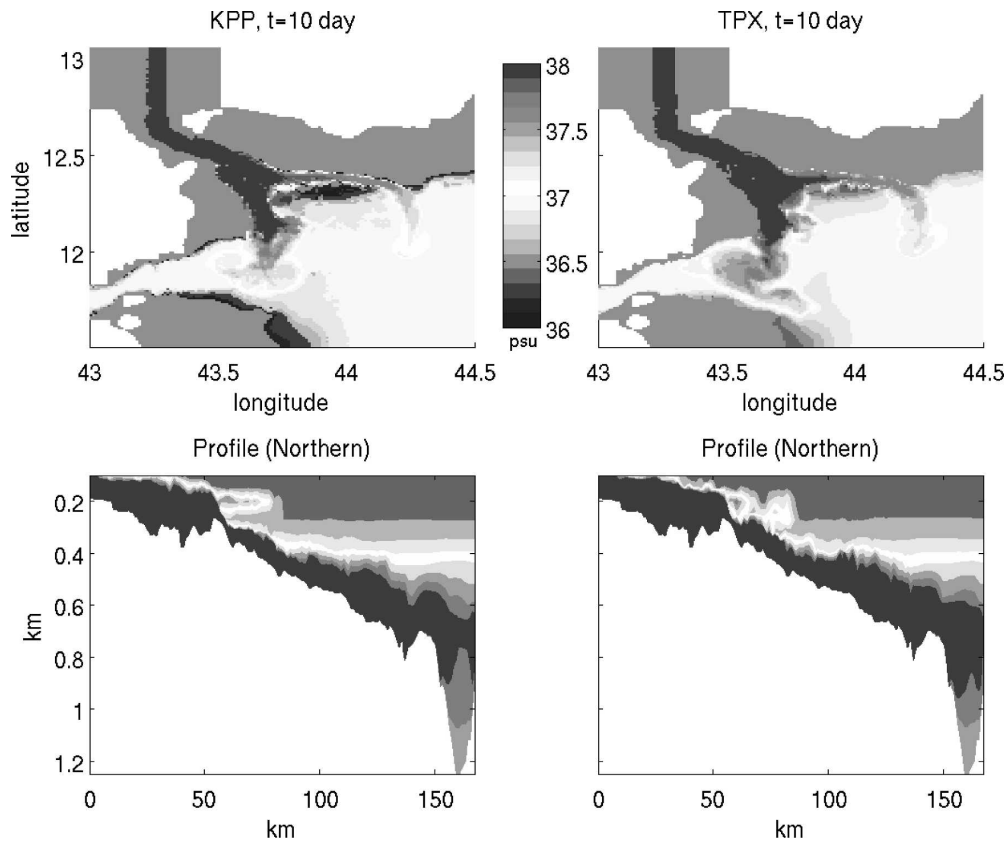


FIG. 16. Comparison of the modeled salinity distribution from (left) KPP and (right) TPX in the (top) plan view (model layer 10) and (bottom) profile view along the northern channel.

$err^i(t)$ is plotted for the eight stations (N1–N5, S1–S3). It can be seen that errors are reduced rapidly until $t = 5$ days, when they drop to less than 10% of the tracer amplitude range, and show little variation after that. Most striking is the similarity of $err^i(t)$ between KPP and TPX. Based on this analysis, the difference in the model results arising from the choice of the vertical mixing parameterization is small compared to other, more significant factors influencing the simulation, namely, the resolution of the details of bottom topography and vertical resolution of the overflow structure.

It should be noted that significant differences have been reported between KPP and TP in the study by Chang et al. (2005) based on an idealized experimental setup in which the slope angle was $\theta = 3.5^\circ$. It was put forth that this was due to the constant value of K_{max} , which was inadequate to provide the mixing needed in the gravity current flow over such slopes. It appears that an order of magnitude smaller slopes in the Red Sea overflow domain, namely, $\theta \approx 1/3^\circ$ in the northern channel, ensure that this limitation of KPP is not encountered in the present simulations.

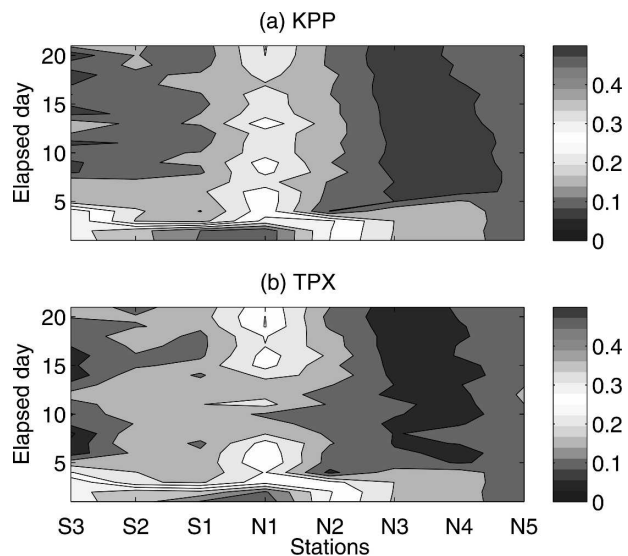


FIG. 17. Time evolution of $err^i(t)$ of computed salinity profiles at eight stations along the northern and southern channels using (a) KPP and (b) TPX.

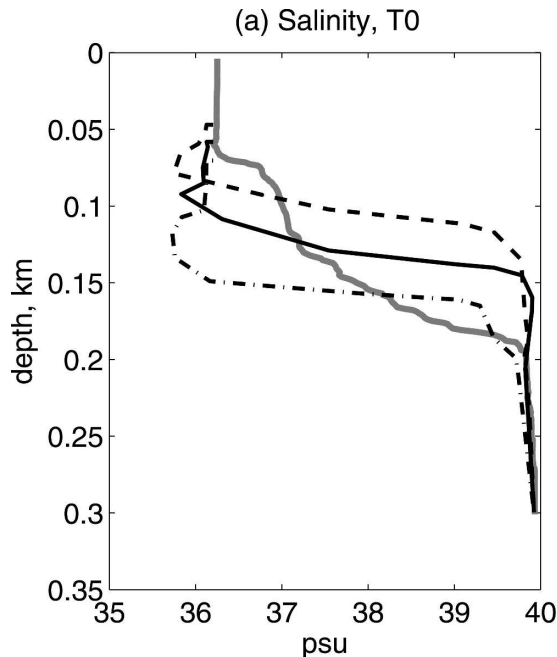


FIG. 18. The modeled salinity profiles at station T0 corresponding to intermediate forcing (black solid line), strong forcing (dashed line), and weak forcing (dashed-dotted line). Gray/solid line shows the REDSOX profile.

g. Sensitivity to source water forcing

Finally, the sensitivity of the results to changes in the inlet source water forcing is explored. This issue is important as the observational sampling in Bab el Mandeb Strait captured neither all the time variability (e.g., due to tides) nor the cross-sectional variations. To develop some insight into consequences associated with uncertainties in source water forcing, two additional experiments are carried out (with TPX and $\Delta x = \Delta y = 1$ km) in which the water mass properties reaching control station T0 are varied. The forcing variation has been accomplished by changing the thickness of the bottom dense water mass inside the artificial reservoir. Figure 18 shows three different levels of outflow water mass at T0. Stronger or weaker forcing is implemented by initializing with approximately $\pm 15\%$ thicker or thinner outflow water height at this station.

The magnitude of this change is somewhat arbitrary as we do not know quantitatively the uncertainties arising from spatial and time sampling. Nevertheless, the change is adequate to provide some insight on the sensitivities of the system to source water forcing. The salinity distributions in the northern channel remain insensitive to the source changes, whereas those in the southern channel exhibit a proportional response (Fig. 19). This response seems a consequence of the implemented source thickness change of ± 25 m (Fig. 18).

This value is of the same order as a 30-m saddle height of the bifurcation point between the channels relative to the floor of the main, northern, channel. A thicker plume will more readily spill over into the southern channel than a thinner one. It is, however, unclear if the OGCM adequately captures the flow dynamics near the bifurcation point. Several factors, such as the need for very high resolution (topography and discretization) and hydraulic control including nonhydrostatic dynamics, need to be considered in future modeling efforts.

5. Summary and discussion

Overflow dynamics constitute an important part of the ocean general circulation since overflows supply most of the intermediate and deep-water masses from spatially restricted source areas, such as narrow straits. In addition, the source water mass properties are typically significantly modified on their path to neutral buoyancy and before joining the general circulation via mixing processes taking place over small spatial and time scales (Price and Baringer 1994). Thus, overflows are considered to form important bottlenecks in the general circulation and need to be explored and understood better in order to be incorporated in OGCMs and ultimately in climate studies in a realistic way.

In this study, realistic simulations of the Red Sea overflow are attempted using HYCOM and observational dataset from REDSOX. To our knowledge, this is the first realistic numerical investigation of the entire Red Sea overflow system. An important objective of this study is to explore the requirements necessary to capture the dynamics of this overflow system using an OGCM. Previous investigations of other overflows revealed significant differences from one another. Computations by Jungclaus and Mellor (2000), Papadakis et al. (2003), and Xu et al. (2006) indicate that the entrainment parameterization is of critical importance in modeling the Mediterranean Sea overflow. Its source water is dense enough to sink to the bottom of the North Atlantic Ocean, but the product waters, in fact, equilibrate at intermediate depths (Baringer and Price 1997a,b). Thus, small differences in entrainment parameterizations are found to lead to significant changes in the properties and equilibrium depth of the product water masses (Xu et al. 2006). In the case of the Denmark Strait overflow, the overflow never detaches from the bottom, and lateral entrainment via quasi-barotropic eddies appears to be important, in addition to vertical entrainment (Käse et al. 2003; T. Haine and A. Adcroft 2006, personal communication). Finescale details of bottom topography appear to exert a strong influence on the overflow in the Faroe Bank Channel (Mauritzen et al. 2005; Ezer 2006), whereas other fac-

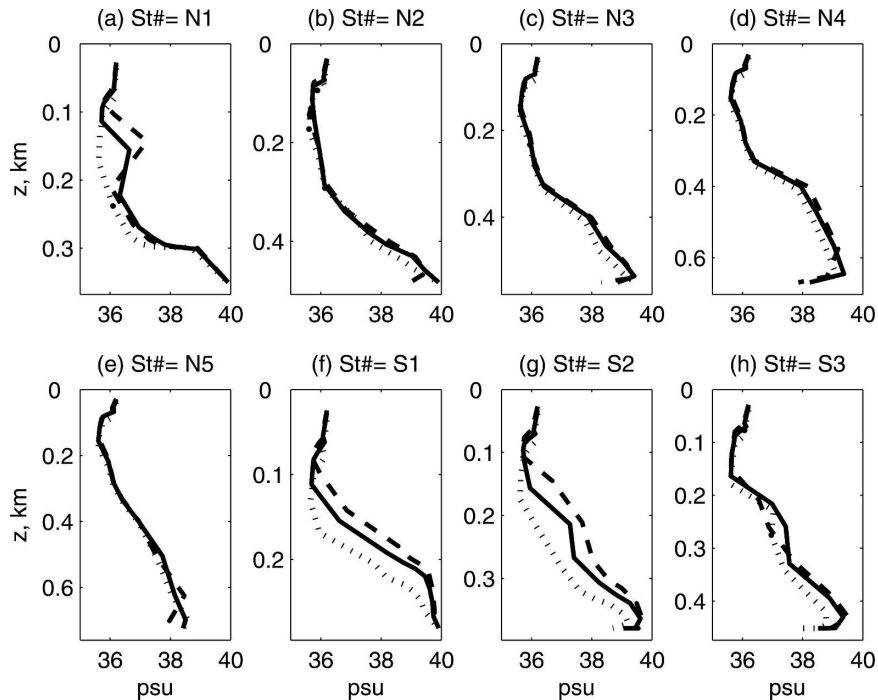


FIG. 19. Sensitivity of modeled salinity profiles in the northern channel (N1–N5) and southern channel (S1–S3) stations to changes in the forcing profiles shown in Fig. 18.

tors such as tidal forcing and formation of episodic cascades seem to be important in the dynamics of Antarctic overflows (Gordon et al. 2004).

The REDSOX dataset is used herein to initialize, force, and validate the model results. In particular, eight stations from the 2001 REDSOX winter cruise are used to assess the model accuracy following bifurcation of the overflow into the narrow channels. Also, three sections crossing the entire overflow system are employed. The comparison of the model results with data is constrained to the phase before the overflows fill the intermediate depths in the Tadjura Rift.

As the simulation is started from a lock exchange at Bab el Mandeb Strait, there is a transient phase of overflow propagation before a statistical steady state is achieved. It is noted that the initial propagation speed of the modeled overflow is much smaller, by a factor of 2 on average, than the theoretical interfacial speed of internal waves. It is shown that this is due to the fact that the initial overflow propagation is impeded by rough topography. A similar effect of rough topography on overflow propagation speed was also noticed in nonhydrostatic simulations by Özgökmen et al. (2004b, their Fig. 2a versus 2d).

A comprehensive comparison of salinity, temperature and velocity profiles, and volume transport in the southern and northern channels, as well as across three

sections crossing the entire overflow system from the model and observations, is carried out. The agreement between the model and data appears reasonably satisfactory. The main contribution of this study is to quantify the sensitivity of the results to various modeling choices. It is found that by far the most important issue in modeling the Red Sea overflow is the resolution of critical topographic features, namely, both the southern and northern channels with their ~ 5 km width, and in particular the area near the bifurcation point of these channels. The popular ETOPO5 dataset contained significant errors, and thus multibeam echo soundings with 200-m resolution were used for these critical areas. A horizontal grid spacing of 1 km, or finer, is required to provide adequate dense water flow into the northern channel and to reproduce a realistic overflow bifurcation and distributions of water mass properties. At coarser resolutions, first the flow in the northern channel and then the southern channel is blocked, and the Red Sea overflow becomes grossly misrepresented. Even with high horizontal resolution, it is a challenge to achieve an accurate partitioning of the flow between the two channels. The narrow multichannel topography significantly increases the challenge of parameterizing entire overflows for climate models in which the typical resolution is 100 km at the present time. Nevertheless, it seems encouraging that the model provides reason-

able results at a marginal resolution of the channels. It is shown that the salinity distributions inside the channels are then affected by the forcing in the strait, such that the modeled dense fluid has a stronger tendency to flow down the southern than the northern channel. A highly accurate topographic dataset and very high model resolution may be required to achieve a higher degree of realism. The importance of the resolution of narrow channels and bottom topography is also evident in the idealized (Ezer 2006) and realistic (Rienschneider and Legg 2007) numerical studies of the Faroe Bank Channel overflow. Alternatively, missing dynamics, such as time-dependent forcing and nonhydrostatic effects, may play an important role near the bifurcation point. Unlike in previous studies of other overflows (e.g., Papadakis et al. 2003; Chang et al. 2005; Xu et al. 2006), the sensitivity of the simulations to the choice of the entrainment parameterization, either TPX or KPP, is found to be small. Nevertheless, a realistic entrainment parameterization is still needed. It is estimated that the volume transport of the overflow increases from 0.41 Sv to 0.55 Sv from section 1 to 3, in approximate agreement with the estimates from observations.

This study indicates that a number of challenges remain in modeling overflows. The first is the challenge of parameterizing the effect of the Red Sea overflow on the general circulation, since it is not feasible in the foreseeable future that the finescale channels will be resolved in climate studies. Thus it is not clear how the effect of topographic pathways can or should be lumped into mixing parameterizations. The second is the inefficiency of numerical methods based on finite-difference schemes when extreme situations are encountered in which the dynamics are constrained to very small areas (channels) whereas computations remain distributed. Alternative numerical methods with higher geometrical flexibility, for example, those based on the finite-element method with adaptive or unstructured grids, should also be considered. The third is the methodological question of assessing the fidelity of a numerical simulation from typically small, sparse, and nonsynoptic observational datasets. Methods for incorporating the uncertainty in the subsampling and time-space variability of observational data in assessing the fidelity of a numerical simulation need to be developed.

Acknowledgments. We greatly appreciate the support of National Science Foundation via Grant OCE 0336799 for the Climate Process Team on Gravity Current Entrainment, as well as through OCE-9819506, OCE-9818464, and OCE-0351116 for the REDSOX. The multibeam echo sounder data from the R/V

L'Atlante were generously provided by Philippe Huchon. These, as well as the echo soundings from the two REDSOX cruises on the R/V *Knorr* and the R/V *Maurice Ewing*, were worked up and kindly shared with us by Steve Swift. We thank Silvia Matt for helping us with merging the high-resolution and low-resolution bottom topography datasets, and Bill Johns and Marcello Magaldi for their constructive criticism. We also thank the two anonymous reviewers for their constructive comments, which greatly helped to improve the manuscript.

REFERENCES

- Baines, P. G., 2001: Mixing in flows down gentle slopes into stratified environments. *J. Fluid Mech.*, **443**, 237–270.
- , 2005: Mixing regimes for the flow of dense fluid down slopes into stratified environments. *J. Fluid Mech.*, **538**, 245–267.
- Baringer, M. O., and J. F. Price, 1997a: Mixing and spreading of the Mediterranean outflow. *J. Phys. Oceanogr.*, **27**, 1654–1677.
- , and —, 1997b: Momentum and energy balance of the Mediterranean outflow. *J. Phys. Oceanogr.*, **27**, 1678–1692.
- Bleck, R., 2002: An oceanic general circulation model framed in hybrid isopycnic-Cartesian coordinates. *Ocean Modell.*, **4**, 55–88.
- Bower, A. S., H. D. Hunt, and J. F. Price, 2000: Character and dynamics of the Red Sea and Persian Gulf outflows. *J. Geophys. Res.*, **105**, 6387–6414.
- , D. M. Fratantoni, W. E. Johns, and H. Peters, 2002: Gulf of Aden eddies and their impacts on Red Sea Water. *Geophys. Res. Lett.*, **29**, 2025, doi:10.1029/2002GL015342.
- , W. E. Johns, D. M. Fratantoni, and H. Peters, 2005: Equilibration and circulation of Red Sea outflow water in the western Gulf of Aden. *J. Phys. Oceanogr.*, **35**, 1963–1985.
- Britter, R. E., and P. F. Linden, 1980: The motion of the front of a gravity current travelling down an incline. *J. Fluid Mech.*, **99**, 531–543.
- Brydon, D., S. Sun, and R. Bleck, 1999: A new approximation of the equation of state for seawater, suitable for numerical ocean models. *J. Geophys. Res.*, **104**, 1537–1540.
- Cenedese, C., J. A. Whitehead, T. A. Ascarelli, and M. Ohiwa, 2004: A dense current flowing down a sloping bottom in a rotating fluid. *J. Phys. Oceanogr.*, **34**, 188–203.
- Chang, Y. S., X. Xu, T. M. Özgökmen, E. P. Chassignet, H. Peters, and P. F. Fischer, 2005: Comparison of gravity current mixing parameterizations and calibration using a high-resolution 3D nonhydrostatic spectral element model. *Ocean Modell.*, **10**, 342–368.
- Chassignet, E. P., L. T. Smith, G. R. Halliwell, and R. Bleck, 2003: North Atlantic simulations with the Hybrid Coordinate Ocean Model (HYCOM): Impact of the vertical coordinate choice, reference pressure, and thermobaricity. *J. Phys. Oceanogr.*, **33**, 2504–2526.
- Ellison, T. H., and J. S. Turner, 1959: Turbulent entrainment in stratified flows. *J. Fluid Mech.*, **6**, 423–448.
- Ezer, T., 2005: Entrainment, diapycnal mixing and transport in three-dimensional bottom gravity current simulations using the Mellor-Yamada turbulence scheme. *Ocean Modell.*, **9**, 151–168.
- , 2006: Topographic influence on overflow dynamics: Idealized numerical simulations and the Faroe Bank Channel overflow. *J. Geophys. Res.*, **111**, C02002, doi:10.1029/2005JC003195.

- , and G. L. Mellor, 2004: A generalized coordinate ocean model and a comparison of the bottom boundary layer dynamics in terrain-following and in z-level grids. *Ocean Modell.*, **6**, 379–403.
- Fernando, H. J. S., 1991: Turbulent mixing in stratified fluids. *Annu. Rev. Fluid Mech.*, **23**, 455–494.
- Girton, J. B., and T. B. Sanford, 2003: Descent and modification of the overflow plume in the Denmark Strait. *J. Phys. Oceanogr.*, **33**, 1351–1364.
- , —, and R. H. Käse, 2001: Synoptic sections of the Denmark Strait overflow. *Geophys. Res. Lett.*, **28**, 1619–1622.
- Gordon, A. L., E. Zambianchi, A. Orsi, M. Visbeck, C. F. Giulivi, T. Whitworth, and G. Spezie, 2004: Energetic plumes over the western Ross Sea continental slope. *Geophys. Res. Lett.*, **31**, L21302, doi:10.1029/2004GL020785.
- Hallberg, R., 2000: Time integration of diapycnal diffusion and Richardson number-dependent mixing in isopycnal coordinate ocean models. *Mon. Wea. Rev.*, **128**, 1402–1419.
- Halliwell, G. R., 2004: Evaluation of vertical coordinate and vertical mixing algorithms in the Hybrid-Coordinate Ocean Model (HYCOM). *Ocean Modell.*, **7**, 285–322.
- Hallworth, M. A., H. E. Huppert, J. C. Phillips, and R. S. J. Sparks, 1996: Entrainment into two-dimensional and axisymmetric turbulent gravity currents. *J. Fluid Mech.*, **308**, 289–311.
- Hébert, H., L. Audin, C. Deplus, P. Huchon, and K. Khanbari, 2001: Lithospheric structure of a nascent spreading ridge inferred from gravity data: The western Gulf of Aden. *J. Geophys. Res.*, **106**, 26 345–26 363.
- Jungclauss, J. H., and G. Mellor, 2000: A three-dimensional model study of the Mediterranean outflow. *J. Mar. Syst.*, **24**, 41–66.
- Käse, R. H., J. B. Girton, and T. B. Sanford, 2003: Structure and variability of the Denmark Strait overflow: Model and observations. *J. Geophys. Res.*, **108**, 3181, doi:10.1029/2002JC001548.
- Killworth, P. D., 1977: Mixing on the Weddell Sea continental slope. *Deep-Sea Res.*, **24**, 427–448.
- Large, W. G., 1998: Modeling and parameterizing ocean planetary boundary layer. *Ocean Modeling and Parameterization*, E. P. Chassignet and J. Vernon, Eds., Kluwer Academic, 45–80.
- , and P. R. Gent, 1999: Validation of vertical mixing in an equatorial ocean model using large eddy simulations and observations. *J. Phys. Oceanogr.*, **29**, 449–464.
- , J. C. McWilliams, and S. C. Doney, 1994: Oceanic vertical mixing: A review and a model with a nonlocal boundary layer parameterization. *Rev. Geophys.*, **32**, 363–403.
- Legg, S., R. W. Hallberg, and J. B. Girton, 2006: Comparison of entrainment in overflows simulated by z-coordinate isopycnal and non-hydrostatic models. *Ocean Modell.*, **11**, 69–97.
- Matt, S., 2004: Transport and entrainment in the Red Sea outflow. M.S. thesis, Department of Meteorology and Physical Oceanography, University of Miami, 93 pp.
- , and W. E. Johns, 2007: Transport and entrainment in the Red Sea outflow plume. *J. Phys. Oceanogr.*, **37**, 819–836.
- Mauritzen, C., J. Price, T. Sanford, and D. Torres, 2005: Circulation and mixing in the Faroese Channels. *Deep-Sea Res. I*, **52**, 883–913.
- Monaghan, J. J., R. A. F. Cas, A. M. Kos, and M. Hallworth, 1999: Gravity currents descending a ramp in a stratified tank. *J. Fluid Mech.*, **379**, 39–70.
- Morcos, S. A., 1970: Physical and chemical oceanography of the Red Sea. *Oceanogr. Mar. Biol. Annu. Rev.*, **8**, 73–202.
- Murray, S. P., and W. Johns, 1997: Direct observations of seasonal exchange through the Bab el Mandab Strait. *Geophys. Res. Lett.*, **24**, 2557–2560.
- Özgökmen, T. M., and E. P. Chassignet, 2002: Dynamics of two-dimensional turbulent bottom gravity currents. *J. Phys. Oceanogr.*, **32**, 1460–1478.
- , W. E. Johns, H. Peters, and S. Matt, 2003: Turbulent mixing in the Red Sea outflow plume from a high-resolution nonhydrostatic model. *J. Phys. Oceanogr.*, **33**, 1846–1869.
- , P. F. Fischer, J. Duan, and T. Iliescu, 2004a: Three-dimensional turbulent bottom density currents from a high-order nonhydrostatic spectral element model. *J. Phys. Oceanogr.*, **34**, 2006–2026.
- , —, —, and —, 2004b: Entrainment in bottom gravity currents over complex topography from three-dimensional nonhydrostatic simulations. *Geophys. Res. Lett.*, **31**, L13212, doi:10.1029/2004GL020186.
- , —, and W. E. Johns, 2006: Product water mass formation by turbulent density currents from a high-order nonhydrostatic spectral element model. *Ocean Modell.*, **12**, 237–267.
- Papadakis, M. P., E. P. Chassignet, and R. W. Hallberg, 2003: Numerical simulations of the Mediterranean Sea outflow: Impact of the entrainment parameterization in an isopycnal coordinate ocean model. *Ocean Modell.*, **5**, 325–356.
- Peters, H., and W. E. Johns, 2005: Mixing and entrainment in the Red Sea outflow plume. Part II: Turbulence characteristics. *J. Phys. Oceanogr.*, **35**, 584–600.
- , —, A. S. Bower, and D. M. Fratantoni, 2005: Mixing and entrainment in the Red Sea outflow plume. Part I: Plume structure. *J. Phys. Oceanogr.*, **35**, 569–583.
- Price, J. F., and M. O. Baringer, 1994: Outflows and deep water production by marginal seas. *Prog. Oceanogr.*, **33**, 161–200.
- Riemenschneider, U., and S. Legg, 2007: Regional simulations of the Faroe Bank Channel overflow in a level model. *Ocean Modell.*, **17**, 93–122.
- Siedler, G., 1969: General circulation of water masses in the Red Sea. *Hot Brines and Recent Heavy Metal Deposits in the Red Sea: A Geochemical and Geophysical Account*, E. T. Degens and D. A. Ross, Eds., Springer-Verlag, 131–137.
- Simpson, J. E., 1969: A comparison between laboratory and atmospheric density currents. *Quart. J. Roy. Meteor. Soc.*, **95**, 758–765.
- , 1982: Gravity current in the laboratory, atmosphere, and ocean. *Annu. Rev. Fluid Mech.*, **14**, 213–234.
- , 1987: *Gravity Currents: In the Environment and the Laboratory*. Halsted Press, 244 pp.
- Smith, W. H. F., and D. T. Sandwell, 1997: Global seafloor topography from satellite altimetry and ship depth soundings. *Science*, **277**, 195–196.
- Sofianos, S. S., W. E. Johns, and S. P. Murray, 2002: Heat and freshwater budgets in the Red Sea from direct observations at Bab el Mandeb. *Deep Sea-Res. II*, **49**, 1323–1340.
- Strang, E. J., and H. J. S. Fernando, 2001: Turbulence and mixing in stratified shear flows. *J. Fluid Mech.*, **428**, 349–386.
- Turner, J. S., 1986: Turbulent entrainment: The development of the entrainment assumption, and its application to geophysical flows. *J. Fluid Mech.*, **173**, 431–471.
- Willebrand, J., and Coauthors, 2001: Circulation characteristics in three eddy-permitting models of the North Atlantic. *Prog. Oceanogr.*, **48**, 123–161.
- Xu, X., Y. S. Chang, H. Peters, T. M. Özgökmen, and E. P. Chassignet, 2006: Parameterization of gravity current entrainment for ocean circulation models using a high-order 3D nonhydrostatic spectral element model. *Ocean Modell.*, **14**, 19–44.